

Active micro-structured arrays for X-ray optics

Alan Michette,^a Tim Button,^b Camelia Dunare,^c Charlotte Feldman,^d Melvyn Folkard,^e
David Hart,^e Chris McFaul,^a Graeme R Morrison,^a William Parkes,^c Sławka Pfauntsch,^a
A. Keith Powell,^a Daniel Rodriguez-Sanmartin,^b Shahin Sahraei,^a Tom Stevenson,^c
Boris Vojnovic,^c Richard Willingale^d and Dou Zhang^b

^aKing's College London, Department of Physics, Strand, London WC2R 2LS, UK

^bUniversity of Birmingham, Department of Metallurgy and Materials, Edgbaston,
Birmingham B15 2TT, UK

^cScottish Microelectronics Centre, University of Edinburgh, The King's Buildings,
West Mains Road, Edinburgh EH9 3JF

^dUniversity of Leicester, Department of Physics and Astronomy, Leicester LE1 7RH, UK

^eGray Cancer Institute, Mount Vernon Hospital, Northwood, Middlesex HA6 2JR, UK

ABSTRACT

The UK Smart X-Ray Optics programme is developing the techniques required to both enhance the performance of existing X-ray systems, such as X-ray telescopes, while also extending the utility of X-ray optics to a broader class of scientific investigation. The approach requires the control of the inherent aberrations of X-ray systems using an active/adaptive method. One of the technologies proposed to achieve this is micro-structured optical arrays, which use grazing incidence reflection through consecutive aligned arrays of channels. Although such arrays are similar in concept to polycapillary and microchannel plate optics, they are more flexible. Bending the arrays allows variable focal length, while flexing parts of them provides adaptive or active systems. Custom configurations can be designed, using ray tracing and finite element analysis, for applications from sub-keV to several-keV X-rays. The channels may be made using deep silicon etching, which can provide appropriate aspect ratios, and flexed using piezo actuators. An exemplar application will be in the micro-probing of biological cells and tissue samples using Ti K_α radiation (4.5 keV) in studies related to radiation induced cancers.

Keywords: X-ray reflection, grazing incidence, active/adaptive reflectors

1. INTRODUCTION

The idea of micro-structured optical arrays (MOAs) was discussed at a SPIE meeting in 2001⁽¹⁾ and at the international X-ray Microscopy conference in Grenoble in 2002.⁽²⁾ Since then, some progress has been made^(3,4) and further results are presented here. The MOA concept is largely based on polycapillary⁽⁵⁾ and microchannel plate⁽⁶⁾ optics, in which X-rays are guided by *multiple* reflections along a large number of small channels. The main differences in MOAs are that the layout of the channels is more flexible and that there are *single* reflections in successive arrays (normally two). This is shown schematically at the left of figure 1, where X-rays from a point source (at the bottom of the figure) are brought to a (quasi-) point focus at the top by two reflections. A central stop prevents unreflected X-rays from reaching the focus. In practice many more channels would be used. In the case shown the second reflection is from a bent array and, by varying the radius of curvature the focal length can be changed. Of course, in principle and depending on the application, either or both arrays could be bent. The use of two reflections means that the Abbe sine condition can be approximately satisfied, thereby reducing aberrations (in particular coma). A schematic diagram of a possible channel layout is shown in the centre of figure 1; again, in practice, many more channels would be used. Note the supporting spokes, which could be coated with piezo material to actuate the bending, and the radially increasing channel widths. The latter would allow for the radially increasing glancing angle, but in practice is not always necessary — or even possible due to the high aspect ratios (line height to width) that would be required for the inner channels.

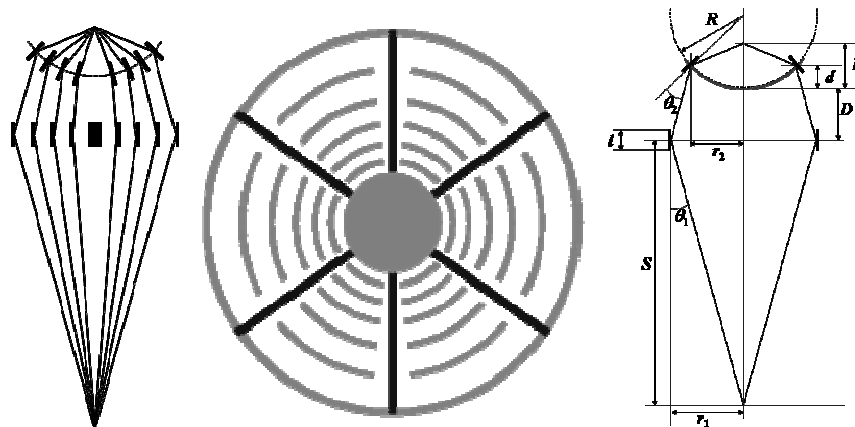


Figure 1. Left: schematic of a two-reflection MOA. Centre: possible channel layout of one of the components. Right: definition of the geometry of a two-reflection MOA.

The geometries of several possible MOA arrangements are discussed in section 2, and in section 3 an analysis is given of an arrangement suitable for focusing X-rays for the micro-probing of biological cells. Modelling of 1D MOA structures by ray tracing and finite element analysis is described in section 4, including the effects of different actuator arrangements. Manufacturing issues including etching of the channels, sidewall roughness and shape, and actuator attachment are discussed in section 5, and some remarks concerning future directions are addressed in section 6.

2. GEOMETRY OF MICRO-STRUCTURED OPTICAL ARRAYS

The geometry of a two-reflection MOA is shown at the right of figure 1; for simplicity, only two pairs of channels, one on either side of the centre, is depicted. Using this geometry, for reflection from the channel centres and assuming a point source, equations (1)–(5) apply. In these, as defined in figure 1, θ_1 and θ_2 are the glancing incidence angles in the first and second components, r_1 and r_2 are the radial distances to the reflecting channel wall, S is the distance from the source to the first component, D is the separation of the (centres of) the two components, d is the vertical distance between the centre and edges of the second component, and F is the focal distance measured from the centre of the second component which is bent to a radius R . Assuming that D and R are set by the user, then solving equations (1)–(3)

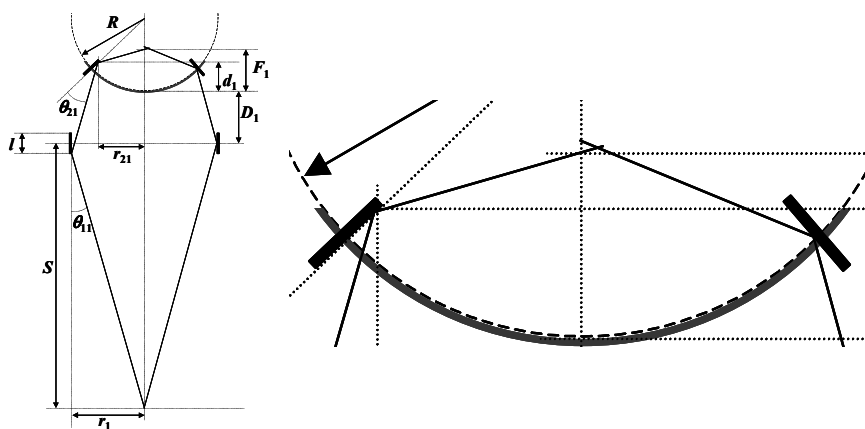


Figure 2. The effect of finite channel length on MOA focusing.

$$\tan \theta_1 = r_1/S \quad (1)$$

$$r_2 = r_1 - (D + d) \tan \theta_1 \quad (2)$$

$$(R - d)^2 + r_2^2 = R^2 \quad (3)$$

allows d and r_2 to be determined for a given r_1 . Then, θ_2 can be calculated from

$$\tan(\theta_1 + \theta_2) = r_2 / (R - d), \quad (4)$$

finally leading to F from

$$\tan(\theta_1 + 2\theta_2) = r_2 / (F - d). \quad (5)$$

These equations do not take into account two effects which will be present in practice. Firstly, not all reflections will be from the channel centres. Radiation incident in a channel of the first component before (after) the centre will have a larger (smaller) grazing incidence angle and will therefore hit the second component channel after (before) the centre, as shown in figure 2, where the left-hand ray hits the first component early in a channel of the first component. The right-hand ray strikes the middle of the channel, for comparison. The result is a broadening of the focal spot, as shown in the blow-up in figure 2. The second effect is due to finite source size, which similarly results in a broadened focal spot.

2.1 Line-to-line MOA focusing

An alternative analysis is to first consider spot-to-spot or, in the simpler case of a linear array of channels, line-to-line focusing, using a single-reflection MOA, as shown schematically in the upper part of figure 3 for an unbent component so that the object and image distances are equal. In the following line-to-line focusing will be analysed; the generalisation to spot-to-spot focusing is obvious via symmetry arguments. The combined reflections from many channels only provide an approximate line focus because the reflecting surfaces are assumed to be planar rather than curved. If the length of the slots is l and the grazing angle is θ then the focused line width will be $\sim l\theta$. The geometry of a single reflection from a channel wall is shown in the lower part of figure 3; the source to MOA distance is s_1 and the MOA to image distance is s_2 . The channel is tilted by an angle φ with respect to the optical axis. If the distance of the channel wall from the axis is h then, using the small angle approximation ($h \ll s_1, s_2$),

$$\frac{h}{s_1} = \theta - \varphi, \quad \frac{h}{s_2} = \theta + \varphi. \quad (6)$$

Eliminating φ leads to

$$\frac{1}{s_1} + \frac{1}{s_2} = \frac{2\theta}{h} = \frac{1}{f} \quad (7)$$

which is the standard Gaussian imaging equation with a focal length $f = h/2\theta$. Eliminating θ from equations (6) gives

$$\frac{1}{s_2} - \frac{1}{s_1} = \frac{2\varphi}{h} \quad (8)$$

leading to the MOA radius of curvature, $R = h/\varphi$,

$$R = \frac{2s_1s_2}{s_1 - s_2}. \quad (9)$$

Note that if $s_2 = s_1$ the radius of curvature is infinite and the MOA is unbent. If the channel width is w then there is a maximum grazing angle of operation, $\theta_{\max} = 2w/l$, assuming parallel walls (figure 4). This, in turn, sets an upper limit to the separation from the optical axis, $h_{\max} = 2s_1w/l$ and hence, assuming no channel curvature, defines the effective f -ratio of the optic, $2h_{\max}/f = 8w/l$. The aperture can be increased by employing a pair of MOAs, as discussed previously, so that the focusing is accomplished by two reflections and the grazing angles on each component are reduced by a factor of approximately two for a given value of h . The increase in the effective aperture depends on the ratio of the grazing angles in the two components.

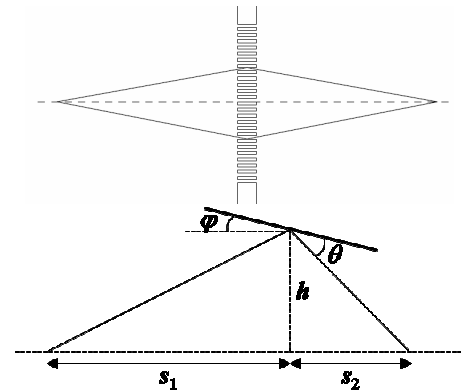


Figure 3. (Top) Grazing incidence reflections from channel walls to provide line-to-line focusing. (Bottom) Geometry of a single reflection.

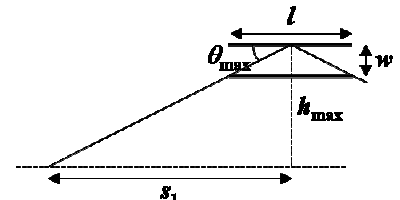


Figure 4. The maximum grazing angle for a channel of length l and width w .

In the following three cases are considered, shown generally in figure 5.

- The grazing angle is the same in each component, which are bent in opposite directions (defined to be negative curvature for the first component and positive for the second). This is likely to yield close to the maximum efficiency for the double reflections which, for linear arrays, produce a line image. The effective aperture will be double that obtained with a single MOA, $2h_{\max}/f = 16w/l$.
- One component is flat and the other is curved, as discussed in the first part of section 2.
- The focal length of the first component is set to the object distance s_1 and that of the second component to the image distance s_2 .

In the third case, the pair forms a collimator–telescope combination; rays passing from the first to the second component are parallel to the optical axis (planar wave fronts). If the channel sizes and spacings are identical for both components then all rays reflected from the first will intersect the reflecting surfaces of the second. However, in the first two cases the rays are converging or diverging and the fraction of rays reflected by the second component will depend on the separation. For the reflections from the two components

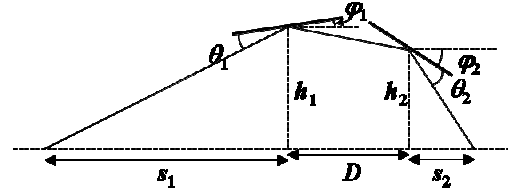


Figure 5. Reflection from a two component MOA.

$$\frac{h_1}{s_1} = \theta_1 + \varphi_1, \quad \frac{h_2}{s_2} = \theta_2 + \varphi_2. \quad (10)$$

2.1.1 Equal grazing angle double-reflection MOA

Setting the grazing angles to be equal (θ), eliminating them from equations (10), using $\varphi_1 = -h_1/R_1$ and $\varphi_2 = h_2/R_2$, and assuming that the component separation $D \ll s_1, s_2$ so that $h_2 \approx h_1 \approx h$, then

$$\frac{1}{R_1} + \frac{1}{R_2} = \frac{1}{s_2} - \frac{1}{s_1}. \quad (11)$$

The included angle between the two components is equal to $\pi - \varphi_1 - \varphi_2$ and to $\pi - 2\theta$. It then follows that

$$\frac{1}{R_2} - \frac{3}{R_1} = \frac{2}{s_1} \quad (12)$$

and solving equations (11) and (12) for the radii of curvature R_1 and R_2 gives

$$R_1 = \frac{4s_1s_2}{s_1 - 3s_2}, \quad R_2 = \frac{4s_1s_2}{3s_1 - s_2}. \quad (13)$$

It can be seen that if $s_1 = s_2 = s$, then $R_1 = -R_2 = -2s$, so that the radii of curvature are equal but with different signs, as expected. The angle between the optical axis and the rays between the two components is $\theta_a = \theta_1 + \varphi_1 = 2h/R_1 + |h/s_1|$.

Substituting for R_1 from equation (11) gives

$$\theta_a = \frac{h}{2} \left(\frac{s_1 - s_2}{s_1s_2} \right). \quad (14)$$

Eliminating φ_1 and φ_2 from equations (10), with equal grazing incidence angles, gives the grazing angle for this configuration,

$$\theta = \frac{h}{4} \left(\frac{s_1 + s_2}{s_1s_2} \right) \quad (15)$$

and the width b of the transmitted beam is

$$b = l\theta = \frac{lh}{4} \left(\frac{s_1 + s_2}{s_1s_2} \right); \quad (16)$$

note that the latter result neglects reflections from the opposite sidewalls, i.e., a non-diverging beam and $s_1, s_2 \gg h$.

So that the rays reflected from the first component are reflected by the second, the gap D between them must be small enough that the rays intersect the width b in the second component, i.e.,

$$D \approx \frac{lh}{4\theta_a} \left(\frac{s_1 + s_2}{s_1 s_2} \right) \quad (17)$$

which gives, substituting for θ_a ,

$$D \approx \frac{l}{2} \left(\frac{s_1 + s_2}{s_1 - s_2} \right). \quad (18)$$

If $s_1 = s_2$ then the rays between the components are parallel and there is no limitation on the gap D .

2.1.2 Flat-curved double-reflection MOAs

With the first component unbent, and the second component bent as discussed in the first part of section 2, equations (10) are still valid but now $\varphi_1 = 0$, corresponding to the required infinite radius of curvature. In addition (figure 5), $\varphi_2 = \theta_1 + \theta_2 = h/R_2$ so that

$$R_2 = \frac{2s_1 s_2}{s_1 + s_2}, \quad (19)$$

noting that $s_1 = 3s_2$ gives $R_1 = \infty$ for the equal grazing angle case, equation (13), and $R_2 = s_1/2$ for the flat-curved combination, equation (19). Satisfying these two requirements simultaneously is a special case for which the first component is flat and the grazing angles are equal in the two components. For the flat-curved combination, $\theta_a = \theta_1$ and equation (18) reduces to the simpler criterion that $D \ll l$ to avoid heavy losses.

2.1.3 Collimator-telescope double-reflection MOAs

In a collimator-telescope configuration the requirements are $R_1 = -2s_1$ and $R_2 = 2s_2$, where the negative sign indicates that the first component is curved with the centre of curvature on the object side so the two components curve in opposite directions. In this configuration the rays in the gap between the components are parallel to the axis so long as R_1 is set correctly and the reflecting surfaces are flat and introduce negligible scatter. The gap between the components can be widened to accommodate other optical elements, such as a grating, and/or support structure without loss in performance.

2.2 Efficiency and resolution

The width b of the beam transmitted through the channels increases linearly with axial offset h until $b = w$, the width of the channel. At this offset the opposite wall of the channel starts to block the inner edge of the beam. As h is increased further the beam width drops linearly until the edge of the useful aperture, given by (for the equal grazing angle case)

$$h_{\max} = \frac{8w}{l} \left(\frac{s_1 s_2}{s_1 + s_2} \right). \quad (20)$$

Note that if $s_1 = s_2$ then h_{\max} is twice that given in section 2.1 for a single MOA; using two reflections doubles the width of the available aperture. The mean beam width across the aperture is $b_{\text{mean}} = w/3$. If the grazing angles are not equal then the beam width will be determined by the smaller of the two angles, which will be less than the grazing angle given by equation (15). Therefore, the width given by equation (16) and the mean value are upper limits.

The geometric area of the double reflection aperture which provides the line-to-line focusing is given by the sum of beam width, w , and the length of the channels across the square aperture, $W = 2h_{\max}$, as a function of h up to h_{\max} . If the channels are evenly spaced with a period p the geometric area is

$$A_{\text{geom}} = \frac{256w^3}{3pl^2} \left(\frac{s_1 s_2}{s_1 + s_2} \right)^2. \quad (21)$$

The effective area is limited by the grazing incidence reflectivity of X-rays from the channel walls. For a given X-ray energy there is a critical angle θ_c for reflection, i.e., the grazing angle below which the reflectivity is high. Efficient use of the channels thus requires $w/l \approx \theta_c$, so that

$$h_{\max} \approx 8\theta_c \left(\frac{s_1 s_2}{s_1 + s_2} \right). \quad (22)$$

So long as channels can be manufactured slots with this aspect ratio (l/w) and over an area of $2h_{\max} \times 2h_{\max}$ then the maximum effective area which can be achieved at the X-ray energy corresponding to the critical angle is

$$A_{\text{eff}} \approx \frac{256\theta_c^2}{3} \frac{w}{p} \left(\frac{s_1 s_2}{s_1 + s_2} \right)^2, \quad (23)$$

assuming that the reflectivity is 100% for $\theta_g < \theta_c$. In practice this is not the case, as due to absorption the reflectivity is only 100% at zero grazing angle for a perfectly smooth surface, and roughness will reduce the reflectivity further. In addition, the aspect ratio corresponding to this effective aperture will be hard to achieve in practice; a silicon surface reflecting titanium K_α X-rays (see section 3) would require $l/w \approx 140$ while in practice (see section 5) ≈ 30 has been achieved in the current work. Thus equation (24) represents an idealised upper limit to the effective area. For a single reflection MOA A_{geom} and A_{eff} are four times smaller than the values given by equations (21) and (23) since all the grazing angles are twice as large and the available aperture is half the size.

For planar walls the individual channels do not provide any focusing, and so if the source line is very narrow the width of the on-axis line from a single channel is

$$\delta = \frac{h s_2}{4} \left(\frac{s_1 + s_2}{s_1 s_2} \right)^2 \quad (24)$$

so that the best resolution (minimum δ) will result from short channels close to the optical axis. However, these channels provide very little effective area. If the aperture is constructed to give the maximum area as described above then the resolution from the combination of channels across the aperture is determined by the average effective beam width $w/3$. A finite source size χ will increase the line focus width by $\chi s_2/s_1$ so that the overall line focus width Δ is the combination of two terms,

$$\Delta \sim \left(\frac{w}{3} \frac{s_1 + s_2}{s_1}, \chi \frac{s_2}{s_1} \right); \quad (25)$$

for Gaussian profiles Δ is given by adding the two terms in quadrature but for other profiles the combination will have a different form.

3. MICRO-PROBING OF BIOLOGICAL CELLS

Any development of new optical components must have the goal of providing new capabilities for applications. In the present case, a significant area of research to be targeted is probing the radiation response of biological material – cells, sub-cellular components and, ultimately, tissue samples – in order to help with the understanding of radiation-induced cancers. Previously,⁽⁷⁾ using focused beams of X-rays from a laboratory source, this has been carried out using (primarily) carbon K X-rays (284 eV) and zone plate optics⁽⁸⁾ to provide micrometre scale focal spots. Although that work has provided very significant results, there are considerable improvements that could be made on at least three fronts. First, carbon K X-rays are almost totally absorbed by single cells, so that tissue samples, of more relevance to living organisms, cannot be studied. Second, to date it has only been possible to study effects leading to cell death rather than the more relevant, for cancer, mutations. This is because for every $\sim 10^4$ cells killed by irradiation only one will mutate, so that many more individual cells must be irradiated. This requirement for high throughput means that the irradiation facility should be available all the time, and so laboratory sources will continue to be used. Finally, in order to irradiate smaller cellular components smaller focal spot sizes will be needed; however, this is unlikely to be achievable in the near future as the focal spot is source-size limited and spot sizes smaller than several micrometres are hard to achieve.

The above arguments indicate that a focusing optic capable of delivering more intensity per unit time than a zone plate (which is limited by its aperture, typically a few hundred micrometres), while providing a focal spot similar in size to that of a zone plate, is required. A higher energy X-ray beam is also needed to allow tissue irradiation, and so a source providing titanium K_α radiation (4.511 keV) is being developed; the higher energy means that the zone plate focal length would be longer ($f \propto E$), providing less demagnification of the source. Preliminary calculations, summarized below, indicate that a MOA with a geometric aperture of ≈ 2 mm, a channel aspect ratio (length:width) of $\approx 20:1$ and a constant period of $20 \mu\text{m}$ in $200 \mu\text{m}$ thick silicon would be suitable, provided that sidewall roughness is no more than a few nanometres.

For the purposes of this example, the optical arrangement of figure 1 was assumed, i.e., a double reflection circular MOA with just the second component bent. The dimensions defined in figure 1 were set at $S=160\text{ mm}$, $D=1\text{ mm}$, $R=100\text{ }\mu\text{m}$ and $l=100\text{ }\mu\text{m}$, resulting in $d\approx 10\text{ }\mu\text{m}$ and $F=72.9\text{ mm}$ — the same as the focal length of a zone plate of diameter $200\text{ }\mu\text{m}$ and outer zone width 100 nm for $\text{Ti K}\alpha$ X-rays. For a point source of $\text{Ti K}\alpha$ X-rays the ray-tracing package Zemax⁽⁹⁾ predicts a MOA focal spot diameter of $\approx 0.2\text{ }\mu\text{m}$ while for a $5\text{ }\mu\text{m}$ source the focal spot diameter is $\approx 2\text{ }\mu\text{m}$; the latter is dominated by the demagnified source size, and so is the same for the zone plate and the MOA. With a smaller bending radius R the value of F for the MOA would be reduced, resulting in a smaller focal spot size. The only way to do this with a zone plate is to use a different optic with either a smaller diameter or a smaller outer zone width. With a sidewall roughness of $\approx 2\text{ nm}$ the MOA provides around two orders of magnitude more focused flux than the corresponding zone plate, primarily due to the larger aperture — the effective aperture diameter is $\approx 1\text{ mm}$ as towards the edge of the optic the grazing angle is larger than the critical angle, so that the reflectivity decreases.

4. FINITE ELEMENT ANALYSIS AND RAY TRACING

Since the MOA channels are made in flat silicon (see section 5) and then bent to give the required focusing and active control, it is necessary to model, using finite element analysis (FEA), the effects of the bending on the channel wall shapes. The results should then be fed into ray-tracing analysis in order to determine the properties of the MOA focus. Section 4.1 describes progress to date on the FEA, and section 4.2 discusses the results of ray tracing of essentially straight channels. The latter uses in-house software as commercial packages are not well suited to MOA structures. The FEA results have not yet been incorporated in the ray tracing.

4.1 Finite element analysis

The FEA, using the commercial package COMSOL Multiphysics,⁽¹⁰⁾ aimed to study the stress and displacement of a 1D MOA when bent by unimorph piezoelectric actuators in different configurations. One quarter of the silicon chip was modelled to take advantage of the symmetry, thus reducing the processing time and allowing finer FEA meshing. The geometry is shown in figure 6, while figures 7–10 show the degree of bending in the x and y directions for different arrangements and thicknesses of the actuators; the effect of glue used to bond the actuators was neglected. The applied voltages were the maximum that the piezos can withstand, namely $\sim 2.5\text{ V}/\mu\text{m}$ of thickness. Clearly, the bending results in very complex shapes, and more detailed analyses are ongoing. One important point that needs to be addressed is that the maximum calculated displacements are smaller than those required in the analyses of sections 3 and 4.2.

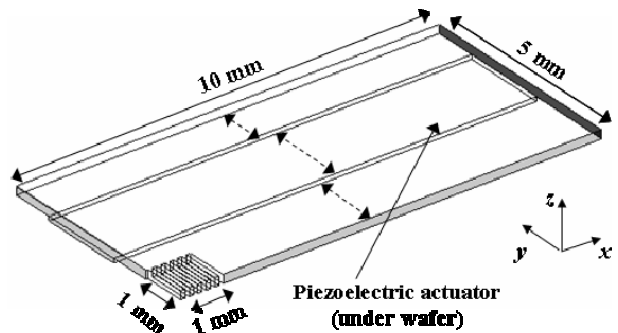


Figure 6. Geometry of a $200\mu\text{m}$ thick 1D MOA chip quarter. The dashed arrows indicate variable dimensions; the piezo thickness is also variable.

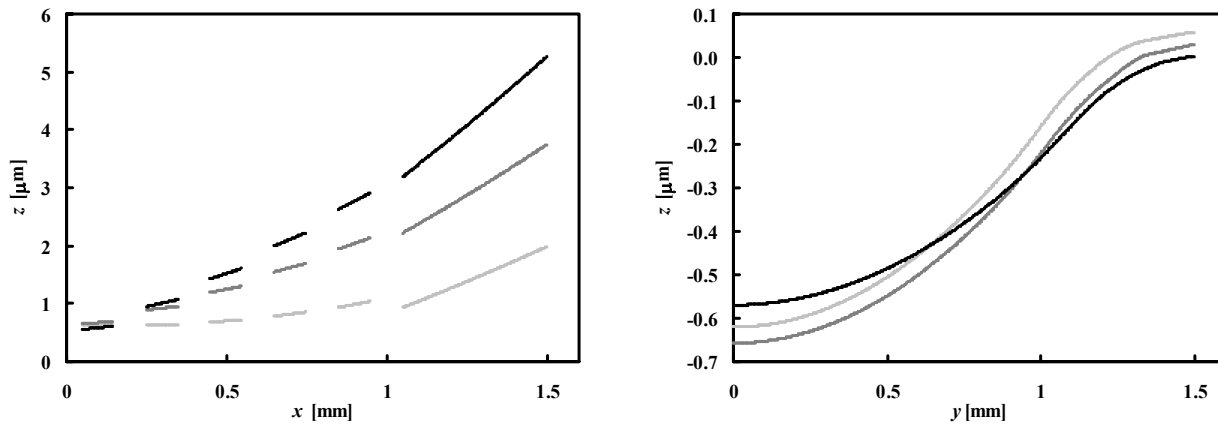


Figure 7. Bending of a 1D MOA actuated by two strips of $150\text{ }\mu\text{m}$ thick PZT-5H placed adjacent to the active area. The dark curve is for strips 4 mm wide, i.e., covering the whole area between the active area and the edge of the silicon chip (see figure 6). The medium and light curves are for strips 2 mm and 1 mm wide respectively. Note the step at the edge of the active area in the x direction.

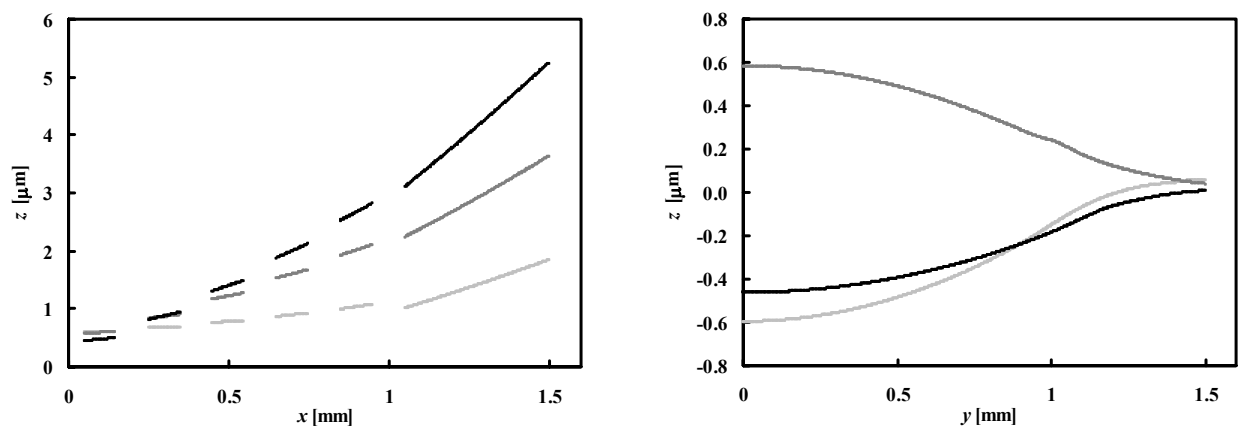


Figure 8. As for figure 7, but with 100 μm thick PZT-5H. Note the reversal of the y -curvature for the 2 mm wide strips; this is presumably due to the relative stiffnesses of the silicon and the piezo, but needs experimental confirmation.

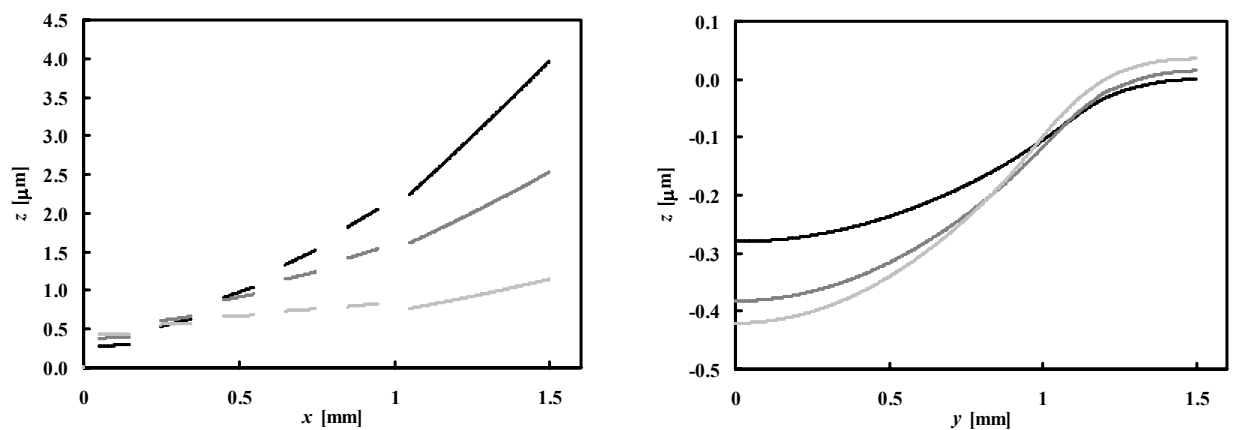


Figure 9. As for figure 7, but with 50 μm thick PZT-5H.

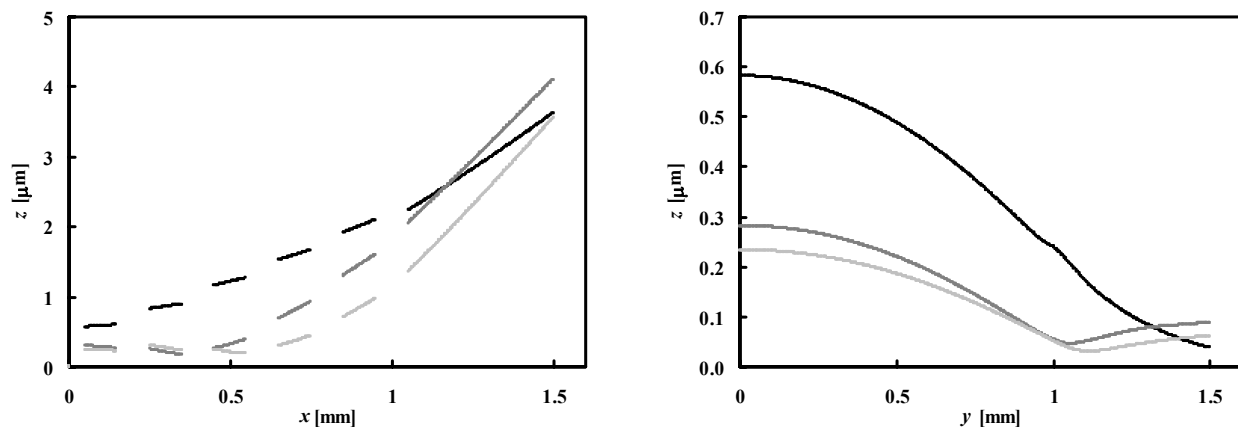


Figure 10. Bending of a 1D MOA actuated by two strips of 100 μm thick, 2 mm wide PZT-5H. The dark curve is for strips placed adjacent to the active area, the medium curve for strips centred between the active area and the edge of the silicon chip, and the light curve for strips placed at the edges of the chip.

4.2 Ray tracing

For the ray tracing described in this section the software “Q”, developed at the University of Leicester specifically for grazing incidence,⁽¹¹⁾ was used. This is much better suited to optics such as MOAs than commercial packages are, and has the flexibility to allow future add-ons, e.g., to take diffraction into account. In this section, for all examples, the rays travel from right to left, and 1D focusing is considered; 2D focusing is readily simulated using cylindrical symmetry. A first example, line-to-line focusing, is shown in figure 11 for a single-reflection MOA with a bending radius of 30 mm.

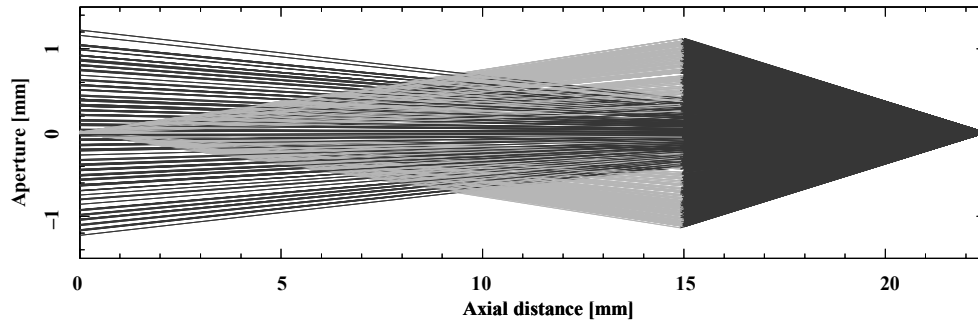


Figure 11. A single-reflection MOA for line-to-line focusing. The darker lines represent rays from the source and those which pass through the optic without reflection. The lighter lines represent the reflected rays.

Figure 12 shows the Q ray tracing for a single-reflection collimator, providing a parallel beam from a diverging source. With the source at a distance of 20 mm, as shown, the required bending radius is 40 mm. Figure 13 shows the reverse optical arrangement, i.e., a single reflection telescope, with the same bending radius.

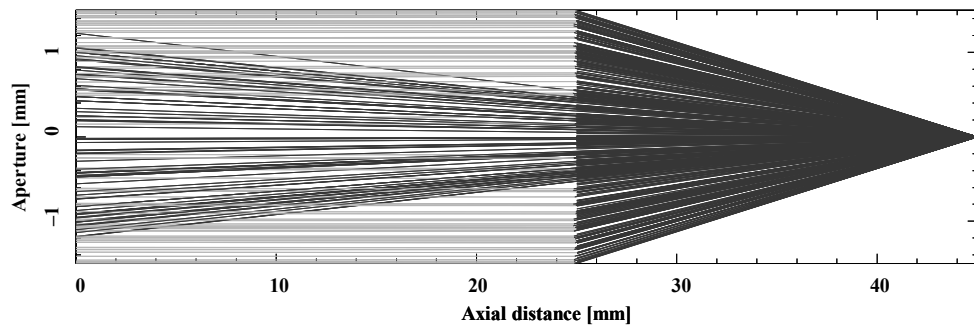


Figure 12. A single-reflection MOA collimator. The darker lines represent rays from the source and those which pass through the optic without reflection. The lighter lines represent the reflected rays.

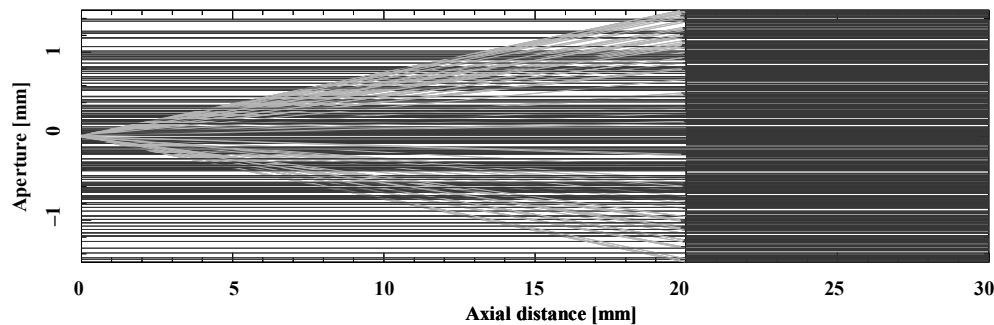


Figure 13. A single-reflection MOA telescope. The darker lines represent rays from the distant source and those which pass through the optic without reflection. The lighter lines represent the reflected rays, brought to a focus.

A double-reflection equal grazing angle MOA is shown in figure 14; this has bending radii $R_1 = 24$ mm and $R_2 = 120$ mm, with opposite curvatures. For a source 15 mm from the optic the double-reflection focus is at 30 mm; the focus due to reflection from just the second component can also be seen, the rays passing straight through the first component.

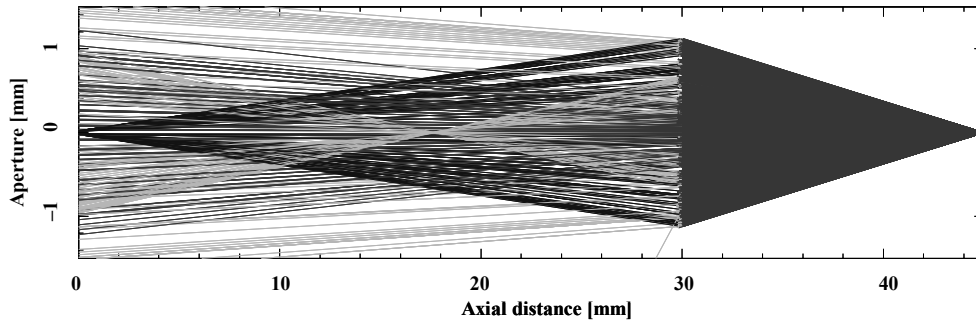


Figure 14. A double-reflection MOA with equal grazing angles in each component. The main focus, at the left, is from the double reflection. The focus, at an axial distance of ≈ 17.5 mm, due to reflection from just the second component can also be seen.

Figure 15 shows a double-reflection flat-curved MOA, the second component having a bending radius of 9.1 mm. Now, there are three foci; the primary double-reflection focus at the left of the figure, that due to reflection from the first component only — off the figure to the left, at a distance equal to the source distance —, and that due to reflection from the second component only. Finally, figure 16 shows the ray-tracing of a double reflection MOA with $s_1 = s_2$, and equal but opposite bending radii of 20 mm, so that the rays between the components are parallel to the axis. Clearly, those rays which reflect from the first component but not from the second remain parallel to the axis; the double-reflection focus and that due to reflection from the second component only can be seen.

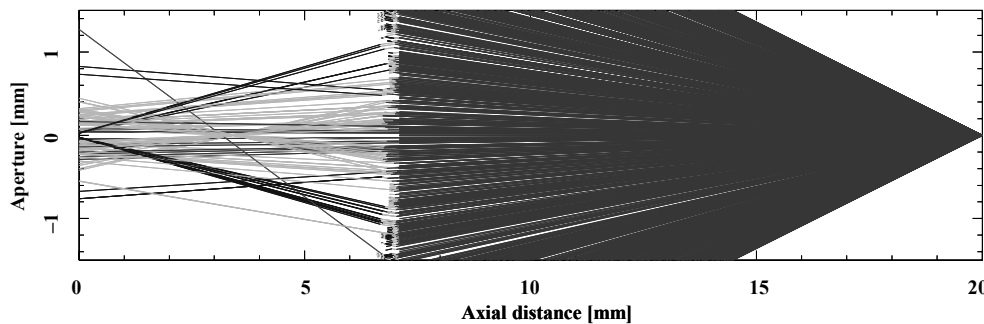


Figure 15. A double-reflection flat-curved MOA, showing three foci. From left to right: that due to reflection from the first component only (off the left of the figure); that due to reflection from both components (at the left of the figure); and that due to reflection from the second component only at an axial distance of ≈ 3.5 mm.

The line spread functions of single- and double-reflection MOAs are shown in figure 17. These plots indicate that, for the double-reflection case, focal sizes in the micrometre range can be obtained, in line with the analysis of section 3.

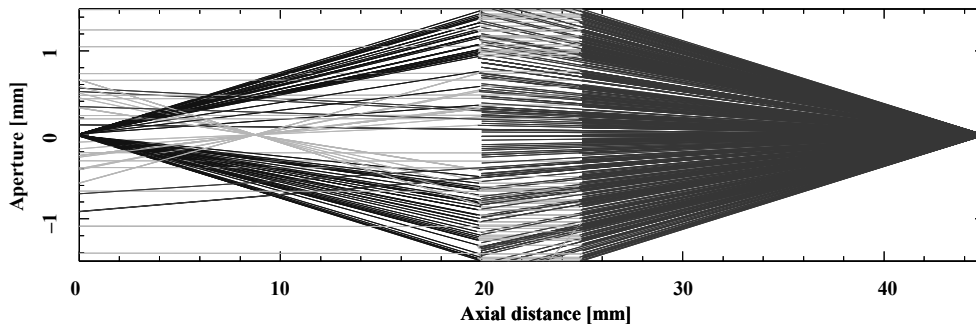


Figure 16. A double-reflection curved-curved MOA, with equal but opposite bending radii.

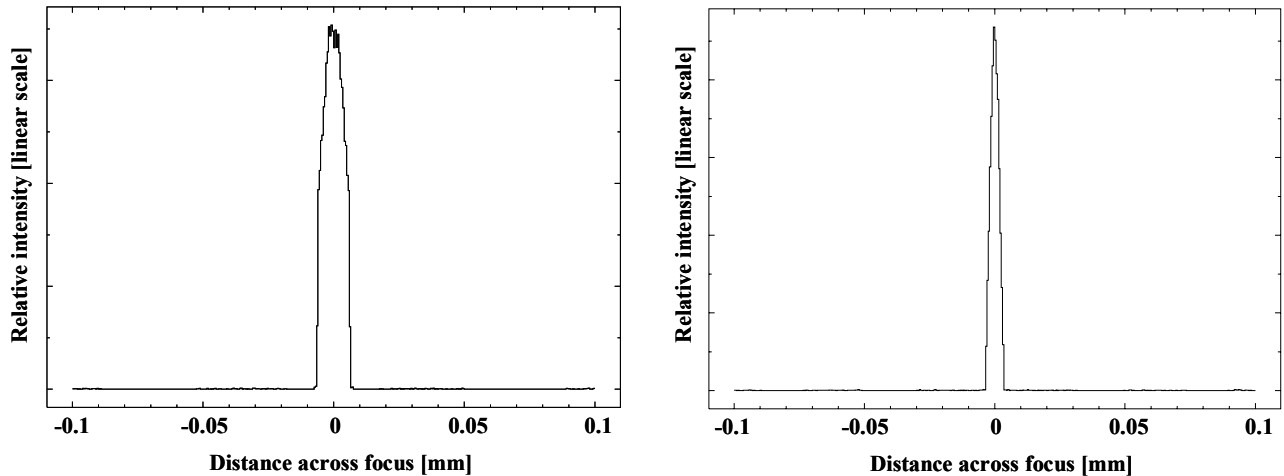


Figure 17. Line spread functions of (left) single-reflection and (right) double-reflection MOAs, determined by Q ray-tracing. The result for the double-reflection case is consistent with the analysis presented in section 3.

5. MANUFACTURING ISSUES

There are two stages in the manufacture the types of optics discussed in the previous section: first, to produce the channel structures and, second, to bond the actuators. To date, only 1D components have been made.

5.1 Deep silicon etching of the channel structures

The route adopted to make the channel structures of the MOAs is deep silicon etching via the Bosch process.⁽¹²⁾ In this, a silicon wafer is patterned through a mask using a cycle of etching/passivation. The gases used are SF₆ and O₂ for etching and C₄F₈ for passivation; the latter prevents sidewall etching and so allows deep channels to be made. However, the channel walls exhibit quasi-periodic peaks and troughs, known as “scalloping”, which, for many applications, is not a significant problem. However, in the present case it is important to minimise the amplitude of these variations to prevent loss of X-rays via scattering; as mentioned in section 3, a root-mean-square (rms) roughness of around 2 nm is required. Roughness can be also caused by non-periodic passivation and etching, which tends to be dominant over the scalloping. There is also the influence of the patterned line edge roughness, but this should not cause x-ray scattering as it is parallel to the lines. Early attempts did not provide roughnesses much better than 10 nm, increasing with channel depth, but a succession of changes to the process cycle have led to values much closer to those required, coupled with deep channels and relatively straight walls (figure 18). The changes include:

- the use of “over-run”, i.e., overlapping the etch and passivate stages, to smooth the peaks and troughs of the scallops;
- reducing and ramping the gas flow, the latter causing pressure variation;
- following etching, the channel walls are subject to oxidation followed by removal, which has the effect of smoothing the peaks.

Using such improvements, local sidewall rms roughnesses of ~4 nm have been achieved, at least in the upper parts of channels; although this is still larger than that required it is likely that further changes to the processes can provide further improvements.

5.2 Actuator control

Several 2×1 cm silicon chips with 2×2 mm active areas have been epoxy bonded to piezo actuators with the general arrangement shown in figure 6; these are awaiting testing. Issues that are being addressed include piezo thickness and width (as discussed in section 4.1), bonding agent thickness and the use of low-shrinkage glues (to prevent shrinking

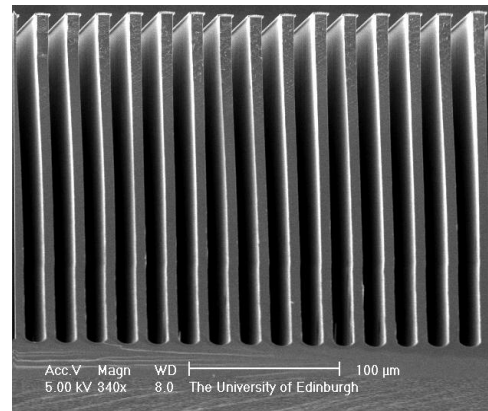


Figure 18. Channels of 20 μ m pitch etched into silicon with an aspect ratio of 18:1 (similar channels with 32:1 have been achieved). The wafer was not fully etched to allow cleaving for inspection by SEM and AFM.

itself causing bending). Different types of actuator, including unimorph (as discussed here), bimorph, and piezo-fibre composites are also being considered.

6. FUTURE WORK

In addition to the future work relating to manufacturing issues referred to in section 5, it will be necessary to consider routes to 2D arrays. One possibility for approximating this will be to use circular arrangements of 1D strips, and it is also intended to investigate the deep etching of circular pattern channels supported by spokes as shown in Figure 1

ACKNOWLEDGEMENTS

The Smart X-Ray Optics consortium is funded by the UK Research Councils' Basic Technology programme, grant code D04880X. The members of the consortium are University College London (including the Mullard Space Science Laboratory), King's College London (KCL), the Gray Cancer Institute (GCI), the University of Leicester, the Scottish Microelectronics Centre at the University of Edinburgh, the University of Birmingham and STFC Daresbury. Silson Ltd. is an associate member. KCL has also received support from the European Science Foundation COST Action P7 "X-Ray and Neutron Optics", while KCL and GCI are supported by the COST Action MP0601 "Short Wavelength Laboratory Sources". Other work of the Smart X-Ray Optics consortium is presented in the paper "Large thin adaptive X-ray mirrors" by Doel *et al.* at this meeting.

REFERENCES

- 1 P.D. Prewett and A.G. Michette, "MOXI: a novel microfabricated zoom lens for x-ray imaging", *Advances in X-Ray Optics*, Proc. SPIE, **4145**, 180–187, (2001)
- 2 A.G. Michette, P.D. Prewett, A.K. Powell, S.J. Pfauntsch, K.D. Atkinson and B. Boonliang, "Novel microstructured adaptive x-ray optics", *J. Phys. IV France*, **104**, 277–280, (2003)
- 3 M.Y. Al Aioubi, P.D. Prewett, S.E. Huq, V. Djakov and A.G. Michette, "Design and fabrication of micro optical system for x-ray analysis of biological cells", *Opto-Ireland 2005: Optoelectronics, Photonic Devices and Optical Networks*, Proc. SPIE, **5825**, 640–646, (2005)
- 4 M.Y. Al Aioubi, P.D. Prewett, S.E. Huq, V. Djakov and A.G. Michette, "A novel MOEMS based adaptive optics for x-ray focusing", *Microelectronic Engineering*, **83**, 1321–1325, (2006)
- 5 C.A. MacDonald and W.M. Gibson, "Applications and advances in polycapillary optics", *X-Ray Spectrometry*, **32**, 258–268, (2003)
- 6 G.J. Price, A.N. Brunton, G.W. Fraser, M. Bavdaz, M.W. Beijersbergen, J.-P. Boutot, R. Fairbend, S.-O. Flyckt, A. Peacock and E. Tomaselli, "Hard X-ray imaging with microchannel plate optics", *Nucl. Instrum. and Methods Phys. Res A*, **490**, 290–298, (2002)
- 7 M. Folkard, K.M. Prise, C. Shao, S. Gilchrist, A.G. Michette AG and B. Vojnovic, "Understanding radiation damage to cells using microbeams", *Acta Physica Polonica A*, **109**, 257–264, (2006)
- 8 A.G. Michette, "X-ray optics", *The Optics Encyclopedia*, Th.G. Brown, K. Creath, H. Kogelnik, M.A. Kriss, J. Schmit and M.J. Weber (Eds), 3305–3371, John Wiley, Berlin, (2003)
- 9 <http://www.zemax.com/>. Last accessed 25 July 2007
- 10 <http://www.comsol.com/>. Last accessed 25 July 2007
- 11 http://www.star.le.ac.uk/~rw/q_v6/index.html. Last accessed 25 July 2007
- 12 F. Laermer, A. Schilp, "Method of anisotropically etching silicon", Robert Bosch GmbH: US Patent 5501893, (1996)